ELSEVIER

J. Non-Newtonian Fluid Mech. 84 (1999) 159–190

Journal of Non-Newtonian Fluid Mechanics

Thermoviscoelastic simulation of thermally and pressure-induced stresses in injection moulding for the prediction of shrinkage and warpage for fibre-reinforced thermoplastics☆

R. Zheng[a,*], P. Kennedy[a], N. Phan-Thien[b], X-J. Fan[b]

[a]*Moldflow Pty. Ltd., 259-261 Colchester Road, Kilsyth, Melbourne VIC. 3137, Australia*
[b]*Department of Mechanical and Mechatronic Engineering, The University of Sydney, Sydney NSW 2006, Australia*

Received 6 March 1998

Abstract

In this paper we present a detailed thermoviscoelastic formulation for the simulation of thermally and pressure induced residual stresses in injection moulded short-fibre-reinforced thermoplastics. The computed residual stresses enable us to predict shrinkage and warpage in the finished products. We also apply an anisotropic version of a rotary diffusion equation to calculate the flow-induced fibre orientation distribution. The predicted fibre orientation state, together with micromechanical theories, allows the incorporation of anisotropy in material properties into the thermoviscoelastic model. Finally we report three numerical examples to indicate the success of the present model.

Keywords: Injection moulding; Residual stresses; Shrinkage; Warpage; Fibre orientation

1. Introduction

Injection moulding of thermoplastics is a widely used technique for producing articles with a high degree of geometrical complexity. A typical injection moulding process consists of four stages: (i) filling of the molten polymer into the mould; (ii) packing of more material into the mould under high pressure to compensate for volumetric shrinkage of the material as it cools; (iii) cooling during which the material solidifies while in the mould until it is sufficiently solid; (iv) ejection of the solidified product from the mould. During filling, packing and cooling, the material experiences a complex thermomechanical history which leads to changes in local specific volume. While the part is in the mould, it is constrained within the plane of the part and so stresses develop in the part during solidification. Upon ejection, the relaxation of these stresses causes instantaneous shrinkage that is usually anisotropic and non-uniform throughout the moulded part. Further shrinkage may also occur

* Corresponding author. Fax: +61-2-9351-7060.
☆ Presented at the 14th TAM Symposium on 'Rheology and Computation', July 1997, Sydney, Australia.

0377-0257/99/$ – see front matter
PII: S0377-0257(98)00148-7

during cooling after ejection. The anisotropic and non-uniform shrinkage behaviour will result in a degree of warpage.

Filling is the most thoroughly studied stage of the injection moulding process. Much of the effort was directed to the prediction of pressure and temperature distributions and the advancement of the melt front [1–6]. Other investigations concentrated on particular features such as the fountain flow [7–13]. Extension of filling analysis to post-filling analysis along with prediction of effective mechanical properties has also been reported (eg., [14] among the others).

Shrinkage and warpage of injection moulded parts have not been so extensively studied as compared with the filling phase, but have received more and more attention recently.

Walsh [15] proposed a correlation for the shrinkage in terms of four variables which represent the effects of pressure–volume–temperature (P–V–T) relation, degree of crystallization, mould restraints and orientation, respectively. These variables can be derived from filling and packing analysis. The correlation involved ten adjustable parameters which depend on material only. The values of these parameters were obtained by fitting the model to experimental shrinkage data measured from moulded specimens of simple geometry. The strains calculated using the 'shrinkage model' were then used in a structural analysis for the calculation of warpage.

A more fundamental approach is based on the relationship between the deformation of the moulded part and the residual stresses built up during the injection process. Thermoelastic or thermoviscoelastic models have been used for the calculation of residual stresses. Residual stresses can be attributed to two sources. First, viscoelastic flow of the polymer during the filling and post-filling stages causes frozen-in flow-induced stresses. Secondly, when the polymer melt is solidified under pressure during the filling, packing and cooling stages, thermal contraction is opposed by the mould and thus the so-called thermally and pressure induced stresses are generated. Usually the flow-induced stresses are relatively small due to rapid relaxation at high temperature and they were often omitted in analyses.

Kabanemi and Crochet [16] reported a numerical study of thermally induced stresses for thermoviscoelastic materials using a three-dimensional finite element method. Material behaviour was assumed to be isotropic. Non-equilibrium behaviour of the polymer during cooling was considered. However, mould constraints to the in-plane shrinkage were not taken into account. The part was treated as a freely quenched body. This essentially leads to neglecting of the packing pressure effect, and as a result they obtained a parabolic distribution of stresses throughout the thickness with compressive stresses at the skin and tensile stresses in the core.

Baaijens [17] employed a compressible Leonov model, also isotropic, to calculate both flow- and thermally-induced stresses under constrained quench conditions, enabling the effect of pressure history to be included. Results showed that the surface region is less compressive and a thin layer close to the skin can be in tension. Along the same lines, Jansen [18], Boitout, et al. [19], Titomanlio and Jansen [20], Zoetelief et al. [21], Caspers [22] and Bushko and Stokes [23–26] conducted either analytical or numerical calculations for the thermally and pressure-induced stresses, using more or less sophisticated constitutive equations (thermo-elastic or thermo-viscoelastic). Their results also showed tensile stresses at the skins of the parts, whatever constitutive models were used.

Isotropic constitutive models are not valid for injection moulded fibre-reinforced composites. Unless the embedded fibres are randomly oriented, they introduce anisotropy in the thermo-mechanical properties of the material. The anisotropic behaviour has a great influence on shrinkage and warpage. The fibre orientation distribution is induced by kinematics of the flow during filling and, to a lesser extent, packing. An extensive literature deals with flow-induced fibre orientation while much other

work has been devoted to micromechanical models which estimate anisotropic elastic and thermal properties of the fibre-matrix system from the properties of the constituent fibre and matrix materials based on given microstructures (comprehensive reviews of both research areas have been given in two recent books edited respectively by Advani [27] and by Papathanasiou and Guell [28] where many references can be found). However, little has been done to relate results from the two research areas and to establish quantitative relationships between the flow-induced fibre orientation and the ultimate dimensional stability of the moulded part. Zheng et al. [29] attempted to relate shrinkage and warpage to the fibre orientation by using micromechanical models together with the P–V–T data to calculate orthotropic thermal strains (instead of stresses). Aspects like mould constraints and viscoelasticity were not considered in the analysis. A similar approach was used previously by Osswald and Tseng [30] for a compression moulding. Rezayat and Stafford [31] presented an anisotropic thermoviscoelastic formulation which was specific to the injection moulding process. However, no numerical results for fibre-reinforced composites were included.

Analysis of the final properties of injection moulded short-fibre composite parts requires accurate prediction of flow-induced fibre orientation. Several different fibre suspension theories and numerical methods are available for the calculation of the motion of fibres during flow. Only the works of Folgar and Tucker [32] and Fan et al. [33] are briefly reviewed here since they are the most relevant. The reader is referred to Phan-Thien and Zheng [34] for additional reviews and discussions on the constitutive theories of fibre suspensions.

Usually, fibre suspensions are classified into three concentration regimes according to the fibre volume fraction, ϕ, and the fibre aspect ratio a_R (defined by the length-to-diameter ratio, L/d). The volume fraction satisfies $\phi = n\pi d^2 L/4$ for rod-like fibres where n is the number density of the fibres. A suspension is called dilute if the volume fraction satisfies $\phi a_R^2 < 1$. In dilute suspensions, each fibre can freely rotate. The region in which $1 < \phi a_R^2 < a_R$ is called semi-concentrated, where each fibre has only two rotating degrees of freedom. Finally, the suspension with $\phi a_R > 1$ is called concentrated, where the average distance between fibres is less than a fibre diameter, and therefore, fibres cannot rotate independently except around their symmetry axes. Any motion of the fibre must necessarily involve a cooperative motion of surrounding fibres. The volume concentration of fibres is also often characterized in terms of nL^3 which approximately equals $4\phi a_R^2/\pi$ for rod-like fibres. Most commercial composites commonly used in injection moulding fall into the semi- or highly-concentrated regimes.

The starting point of Folgar and Tucker's work on fibre suspensions is the evolution equation of Jeffery [35] for the motion of an isolated fibre in a Newtonian fluid. Jeffery's equation is valid for dilute fibre suspensions where there is no fibre–fibre interaction. Folgar and Tucker [32] added a diffusion term to Jeffery's equation to model fibre–fibre interaction. An empirical constant called the interaction coefficient (C_I) is introduced in the diffusion term. The constant C_I for a given suspension is assumed to be isotropic and independent of the orientation state, as a first approximation. The Folgar–Tucker model has extended the fibre orientation simulations into non-dilute regimes. The main uncertainty is the chosen value for the coefficient C_I.

Fan et al. [33] recently presented a direct numerical simulation of fibre–fibre interactions. Short-range interaction is modeled by lubrication forces [36]. Long-range interaction was calculated using a boundary element method. The hydrodynamic force and torque on each fibre were calculated to determine the motion of the fibre. Although the direct simulation method is currently limited to a simple shear flow, the numerical results can be used to produce macroscopic properties of the suspension, including the Folgar–Tucker constant C_I.

In this paper, based on a detailed numerical simulation of the filling, packing, cooling and flow-induced fibre orientation, we present an anisotropic thermoviscoelastic model for the computation of the thermally and pressure-induced stresses in injection moulded fibre-reinforced composites. The flow-induced residual stresses are neglected. The computed stresses are used to predict shrinkage and warpage caused by the relaxation of these stresses after ejection. An anisotropic version of Folgar–Tucker's rotary diffusion equation is used to simulate flow-induced fibre orientation, along with the direct simulation method [33] for the prediction of the interaction coefficient. Mechanical and thermal properties of the composite required for use in the anisotropic thermoviscoelastic constitutive equations are estimated using micromechanical models. Multi-layer shell elements are used, which are capable of solving problems with complex 3-D geometries and thin-walled structures.

2. Problem formulation

2.1. Flow and flow-induced fibre orientation

The governing fluid flow equations to be solved are Momentum:

$$\sigma_{ij,j} = 0, \tag{1}$$

Mass:

$$\frac{D\rho}{Dt} + \rho v_{i,i} = 0, \tag{2}$$

Heat transfer:

$$\rho c_{\mathrm{p}} \frac{\mathrm{D}T}{\mathrm{D}t} = kT_{i,i} + \sigma_{ij} D_{ij} - \frac{T}{\rho}\frac{\partial \rho}{\partial T}\frac{\mathrm{D}p}{\mathrm{D}t} + \rho_{\mathrm{c}} H_{\mathrm{c}} \frac{\partial \chi}{\partial t}, \tag{3}$$

where the Cartesian index notation is used, the repeated indices imply summation, and a comma denotes partial differentiation with respect to the coordinate, D/Dt is the material derivative, σ_{ij} denotes the total stress tensor, $\rho = \rho(T, p)$ represents the fluid density at local temperature (T) and pressure (p), v_i is the velocity vector, c_{p} is the specific heat at constant pressure, k is the thermal conductivity, ρ_{c} is the crystal density, H_{c} is the latent heat of crystallization, χ is crystallinity and D_{ij} is the rate of strain tensor defined as $D_{ij} = (v_{i,j} + v_{j,i})/2$. For semi-crystalline materials, crystallization kinetic equations (e.g., [47]) will be solved together with the above governing equations.

A Cross model is used to model the shear-rate, pressure and temperature dependent viscosity. We assume that the flow field remains unaltered by the orientation distribution of the fibres, and hence the flow computation is essentially de-coupled from the orientation process. The coupled fibre-flow interaction has received considerable attention in numerical simulations of complex flows (see, for example, [37–42]. It is believed that the effects of the fibre motion on the flow kinematics are in general important, especially when there are strong elongational flow components. On the other hand, Tucker [43] has argued that decoupling of orientation and flow is allowed as a special case for a flow through a narrow gap. The condition for the influence of the fibres on the fluid motion to become negligible is $N_{\mathrm{p}}\delta^2 \ll 1$ and $\delta \sim \varepsilon$, where N_{p} is the particle number representing the resistance of the fibre to flow

stretching effects, ε is a geometric parameter defined as the ratio of the gap height to the typical mid-plane dimension, and δ is the order of magnitude of out-of-plane orientation. The condition can be satisfied when the gap is sufficiently narrow because in a very narrow gap the fibres lie down nearly parallel to the mid-plane and therefore the magnitude of δ is very small.

In this paper we consider thin-walled moulded parts characterized by a small thickness as compared to other dimensions. Under such conditions, it is possible to use lubrication approximations in the flow analysis. Pressure variations through the thickness are negligible, and the pressure field satisfies the well-known Hele–Shaw equation of the form:

$$\nabla \cdot (S\nabla p) = \int_{-h/2}^{h/2} \frac{1}{\rho}\frac{\mathrm{D}\rho}{\mathrm{D}t}\,\mathrm{d}x_3 \tag{4}$$

where ∇ denotes the gradient operator with respect to the midplane, S the flow conductance factor which depends on viscosity and the thickness of the cavity, h the thickness of the cavity and x_3 the local thickness coordinate. The Hele–Shaw equation is elliptic in nature, and the boundary conditions are given as either the inlet flow rate or the pressure boundary condition at the gates; a zero pressure, $P = 0$, on the advancing flow front; and a zero normal pressure gradient $\partial P/\partial n = 0$ along the edges of the mould. The no-slip condition is not necessarily satisfied on the edges. Instead, the fluid may 'slip', leading to inaccurate velocity predictions within a thin boundary layer of order h. The accuracy of the Hele–Shaw model used for thin-walled geometries has been justified by Guell and Lovalenti [44].

Fountain flow cannot be represented by the Hele–Shaw approximation since the approximation is a two-dimensional representation ignoring the gapwise transverse flow. Fountain flow is the phenomenon that the material approaching the front free surface is moving from the core to the mould wall while at the same time it is stretched an re-oriented. Therefore neglecting the fountain flow may result in somewhat incorrect predictions of temperature and fibre orientation within the outer surface layer. Local approximate treatments accounting for the effect of fountain flow on temperature and orientation have been reviewed by Crochet et al. [5].

It is customary to use a unit vector $\boldsymbol{p}$ to specify the fibre orientation in suspensions. The probability distribution function of the fibre orientation can be described by the second- and fourth-order orientation tensors $\langle \boldsymbol{pp} \rangle$ and $\langle \boldsymbol{pppp} \rangle$ (or, in Cartesian tensor notation, a_{ij} and a_{ijkl}) where the angular brackets denote the ensemble average with respect to the probability density function.

The Folgar–Tucker model in terms of the orientation tensors can be formulated as follows [45]:

$$\frac{Da_{ij}}{Dt} = \omega_{ik}a_{kj} - a_{ik}\omega_{kj} + \lambda\left(D_{ik}a_{kj} + a_{ik}D_{kj} - 2D_{kl}a_{ijkl}\right) + 2C_{\mathrm{I}}\dot{\gamma}\left(\delta_{ij} - \alpha a_{ij}\right) \tag{5}$$

where λ is a function of the fibre aspect ratio defined as $(a_{\mathrm{R}}^2 - 1)/(a_{\mathrm{R}}^2 + 1)$, ω_{ij} the local vorticity (defined as $\omega_{ij} = (v_{i,j} - v_{j,i})/2$) and D_{ij} the rate of strain tensors as defined before, $\dot{\gamma}$ is the generalized shear rate defined as $\dot{\gamma}^2 = 2D_{ij}D_{ij}$, δ_{ij} the Kronecker delta and α a constant that equals 3 for three-dimensional orientation and 2 for planar orientation to satisfy the condition $\mathrm{Tr}\langle \boldsymbol{pp} \rangle = 1$. The coefficient C_{I} introduced by Folgar and Tucker [32] is a measure of the intensity of fibre interactions in the suspension. In this work we perform a three-dimensional orientation calculation. We believe that the three-dimensional calculation provides more accurate results than the two-dimensional calculation, although the latter requires less computing time (In the 2-D calculation it is necessary to impose artificial values of out-of-plane fibre orientation components, otherwise it will predict incorrect results of the in-plane orientation).

A closure approximation is needed to express the fourth-order tensor in terms of the second-order tensor. There are several different forms of closure approximations proposed. The widely used ones are quadratic [46], hybrid [45] and composite [48] approximations. More recently a new type of closure approximation based on fitting particular solutions to the solutions of the probability density function in a few well-defined flow fields has been proposed. These include the natural closure by Verleye and Dupret [49] and the orthotropic closure by Cintra and Tucker [50]. A variety of other closure approximations are also available. It is known that the validity of the closure schemes depends on the type of flow and the degree of alignment of the fibres. We use the orthotropic closure approximation in this work.

A difficulty with the use of the Folgar–Tucker model is the determination of the C_I value. Bay [51] suggested an empirical expression for C_I (as a function of ϕa_R) which was obtained by matching numerical solutions with experimental data. In the present work we use the direct simulation method developed by Fan et al. [33] to model the fibre–fibre interaction for a simple shear flow. The orientation $\boldsymbol{p}$ of each fibre depends only on its initial configuration, its aspect ratio, the number density of fibres in the suspension and the shear deformation. The components of both the second- and fourth-order tensors a_{ij} and a_{ijkl} can be obtained by an appropriate averaging procedure. Numerical values of a_{ij} and a_{ijkl} are then used in an anisotropic version of Folgar–Tucker's rotary diffusion equation to determine the interaction coefficient in the defined shear flow. The anisotropic version of Folgar–Tucker's equation is given by

$$\frac{Da_{ij}}{Dt} = \omega_{ik}a_{kj} - a_{ik}\omega_{kj} + \lambda\left(D_{ik}a_{kj} + a_{ik}D_{kj} - 2D_{kl}a_{ijkl}\right) - 3\dot{\gamma}\left(C_{jk}a_{kj} + C_{jk}a_{ik}\right) + 6\dot{\gamma}C_{kl}a_{ijkl} + 2\dot{\gamma}\left(C_{ij} - C_{kk}a_{ij}\right), \tag{6}$$

Here, the isotropic diffusivity $C_I\delta_{ij}$ in the original Folgar–Tucker model has been extended to a symmetrical second-order tensor C_{ij} to take into account anisotropic behaviour. The motivation for using the anisotropic diffusivity is the fact that the numerical solutions of the direct simulation do not support the isotropic diffusion assumption. Once all components of the moment tensors are obtained from the direct simulation, six components of the tensor C_{ij} can be determined by using Eq. (6) for the shear flow. Eq. (6) with the tensor C_{ij} thus determined can then be used to simulate the evolution of fibre orientation in injection moulding. If the three eigenvalues of the tensor C_{ij} are identical, then the diffusivity is isotropic and C_I equals the eigenvalue.

2.2. Equation of state

For the analysis of the packing phase, the governing equations are the same as those in the filling phase. However, it is essential to include the effect of melt compressibility. An equation of state, i.e., the so-called P–V–T relation, is required for treating the compressibility. The P–V–T relation considers the specific volume of a material as a function of temperature, pressure, and cooling rate, i.e.,

$$\hat{V} = \hat{V}\left(p, T, \frac{\partial T}{\partial t}\right), \tag{7}$$

where $\hat{V}$ is the specific volume.

Semi-crystalline polymers are more sensitive to changes in cooling rate than amorphous polymers. The crystallization temperature decreases with increasing cooling rate. In numerical simulation, the equilibrium P–V–T relation of the semi-crystalline material can be shifted down in temperature to model the behaviour at higher cooling rate, based on experimental observation or the crystalline kinetics. For amorphous materials, we use a quasi-equilibrium assumption and neglect the cooling-rate effect.

Important material properties such as volume thermal expansion coefficients and compressibility can be derived from the equation of state as functions of temperature and pressure. The P–V–T relation can also be used for detection of transitions between polymer states, such as freezing and melting, crystallization, and glass transition phenomena.

2.3. Mechanical and thermal properties

An elastic anisotropic material generally needs 21 constants for a full characterization. If viscoelastic, this means 21 material functions of time. A material is called transversely isotropic if its properties are equal in two dimensions but different in the third. Such material requires five independent material constants or functions. Unidirectional fibre-reinforced composites can be classified as transversely isotropic materials.

In order to predict the effective elastic and thermal properties of the short-fibre reinforced composites, we follow a two-step procedure. First, we estimate the unidirectional properties assuming the fibres are fully aligned. Secondly, an orientation averaging procedure is applied to consider the fibre orientation distribution.

The first step is achieved by means of micromechanical models. The Tandon–Weng model [52] is used to determine five elastic moduli associated with transversely isotropic composites where the axis normal to the isotropic plane is coincident with the fibre axis, i.e., the 1-direction, while the 2–3 directions define the plane of isotropy. The five elastic moduli are the longitudinal Young's modulus E_{11}, the transverse Young's modulus E_{22}, the in-plane shear modulus G_{12}, the out-plane shear modulus G_{23}, and the plane-strain bulk modulus K_{23}. The Poisson ratios ν_{12}, ν_{21}, and ν_{23} are not independent properties; they are related to others. The Tandon–Weng equations are too tedious to rewrite here; the user is referred to the original paper [52] for details.

Schapery [53] proposed an expression for longitudinal and transverse thermal expansion coefficients (denoted as α_1 and α_2, respectively) of unidirectional fibre-reinforced composites with isotropic fibres embedded in an isotropic matrix based on energy considerations. The expressions are used in this work in the following form:

$$\alpha_1 = \frac{E_f \alpha_f \phi + E_m \alpha_m (1-\phi)}{E_f \phi + E_m (1-\phi)} \tag{8}$$

and

$$\alpha_2 = (1+\nu_m)\alpha_m(1-\phi) + (1+\nu_f)\alpha_f\phi - \alpha_1\nu_{12}, \tag{9}$$

where subscripts 'f' and 'm' denote fibre and matrix, respectively, E the Young's modulus and ν the Poisson ratio.

Table 1
Summary of the relationship between the contracted and tensor notations

Contracted notation	Tensor notation
1	11
2	22
3	33
4	23
5	13
6	12

For an anisotropic elastic solid, Hooke's law can be written as

$$\sigma_{ij} = c^{(e)}_{ijkl}\,\varepsilon_{kl}, \tag{10}$$

where σ_{ij} and ε_{kl} are the stress and strain tensors, respectively. The strain tensor is determined from derivatives of the displacements $\boldsymbol{u}$ as $\varepsilon_{ij} = \frac{1}{2}(u_{i,j} + u_{j,i})$, and $c^{(e)}_{ijkl}$ is the elastic constant tensor called the stiffness tensor. It is common to use a contracted notation for Eq. (10) and to write it as

$$\sigma_m = c^{(e)}_{mn}\,\varepsilon_n, \tag{11}$$

where $m, n = 1, 2, 3, 4, 5, 6$. The relationship between the contracted notation and the tensor notation is tabulated in Table 1.

In matrix form the equation for a transversely isotropic material with the axis of material symmetry coincident with the 1-direction is

$$\begin{pmatrix} \sigma_1 \\ \sigma_2 \\ \sigma_3 \\ \sigma_4 \\ \sigma_5 \\ \sigma_6 \end{pmatrix} = \begin{pmatrix} c^{(e)}_{11} & c^{(e)}_{12} & c^{(e)}_{12} & 0 & 0 & 0 \\ c^{(e)}_{12} & c^{(e)}_{22} & c^{(e)}_{23} & 0 & 0 & 0 \\ c^{(e)}_{12} & c^{(e)}_{23} & c^{(e)}_{22} & 0 & 0 & 0 \\ 0 & 0 & 0 & c^{(e)}_{44} & 0 & 0 \\ 0 & 0 & 0 & 0 & c^{(e)}_{55} & 0 \\ 0 & 0 & 0 & 0 & 0 & c^{(e)}_{66} \end{pmatrix} \begin{pmatrix} \varepsilon_1 \\ \varepsilon_2 \\ \varepsilon_3 \\ \varepsilon_4 \\ \varepsilon_5 \\ \varepsilon_6 \end{pmatrix} \tag{12}$$

in which $c^{(e)}_{44} = \frac{1}{2}\left(c^{(e)}_{22} - c^{(e)}_{23}\right)$ and $c^{(e)}_{55} = c^{(e)}_{66}$. In terms of the engineering quantities the components of the stiffness matrix are given by [54]

$$c^{(e)}_{11} = \frac{(1-\nu_{23})E_{11}}{1-\nu_{23}-2\nu_{12}\nu_{21}}, \tag{13}$$

$$c^{(e)}_{12} = \frac{\nu_{21}E_{11}}{1-\nu_{23}-2\nu_{12}\nu_{21}}, \tag{14}$$

$$c^{(e)}_{22} = \frac{E_{22}}{2(1-\nu_{23}-2\nu_{12}\nu_{21})} + G_{23}, \tag{15}$$

$$c^{(e)}_{23} = \frac{E_{22}}{2(1-\nu_{23}-2\nu_{12}\nu_{21})} - G_{23}, \tag{16}$$

$$c_{55}^{(e)} = G_{12} \tag{17}$$

Note that in Eq. (12), $\varepsilon_1 = \varepsilon_{11}$, $\varepsilon_2 = \varepsilon_{22}$, $\varepsilon_3 = \varepsilon_{33}$, while $\varepsilon_4 = 2\varepsilon_{23}$, $\varepsilon_5 = 2\varepsilon_{13}$ and $\varepsilon_6 = 2\varepsilon_{12}$.

In the second step, we compute the orientation averages using the predicted orientation tensors. The relevant results are, according to Advani and Tucker [45]:

$$\langle c_{ijkl}^{(e)} \rangle = B_1 a_{ijkl} + B_2(a_{ij}\delta_{kl} + a_{kl}\delta_{ij}) + B_3(a_{ik}\delta_{jl} + a_{il}\delta_{jk} + a_{jl}\delta_{ik} + a_{jk}\delta_{il}) + B_4\delta_{ij}\delta_{kl} + B_5(\delta_{ik}\delta_{jl} + \delta_{il}\delta_{jk}) \tag{18}$$

and

$$\langle \alpha_{ij} \rangle = (\alpha_1 - \alpha_2)a_{ij} + \alpha_2\delta_{ij}. \tag{19}$$

where the five constants B_i's are invariants of the unidirectional property tensor; they can be calculated from the unidirectional properties of the transversely isotropic material [45].

The orientation averaging procedures expressed by Eq. (18) and Eq. (19) fall into the category of the so-called bounding approach. The composite is thought to be an aggregate assembled by discrete material elements, each of which contains the matrix and fully aligned fibres. One can derive different averaging formulations based on different assumptions for the distribution of strain and stress field throughout the aggregate. It is easy to show that the orientation average of the thermal expansion calculated, as shown in Eq. (19), corresponds to the effective thermal expansion based on the assumption of a uniform stress and a constant ΔT (temperature difference) throughout the aggregate. Alternatively, if the strain is assumed to be uniform, the corresponding averaging formulation is different (see, for example, [55]). Eduljee et al. [56] have proposed other averaging approaches which are more sophisticated than the bounding approach.

In Eqs. (18) and (19) the angular brackets denote the orientation average. In what follows we will drop out the angular brackets. It is noted that the material properties are not necessarily transversely isotropic after orientation averaging.

2.4. Anisotropic thermoviscoelastic model

Thermally and pressure induced stresses arise from inhomogeneous cooling of the part in combination with the hydrostatic pressure. Upon cooling, the relaxation time increases and becomes comparable to the process time, therefore accurate predictions of thermal stresses would require viscoelastic constitutive equations. In the limit of infinitesimal strains the behaviour of viscoelastic materials is well described by the theory of linear viscoelasticity [57,58]. A linear anisotropic thermoviscoelastic constitutive equation can be written as

$$\sigma_{ij} = \int_0^t c_{ijkl}(\xi(t) - \xi(t'))\left(\frac{\partial \varepsilon_{kl}}{\partial t'} - \alpha_{kl}\frac{\partial T}{\partial t'}\right) \mathrm{d}t' \tag{20}$$

where $c_{ijkl}(t)$ is the viscoelastic relaxation modulus. In the formulation it is assumed that the material is undisturbed for all $t < 0$.

In Eq. (20) $\xi(t)$ is a pseudo-time scale given by

$$\xi(t) = \int_0^t \frac{1}{a_T}\,\mathrm{d}t' \tag{21}$$

where a_T is the time–temperature shift factor that reflects the effect of temperature on the material response.

For amorphous materials with temperatures raging from T_g to $T_g + 100°C$, where T_g is the glass transition temperature, the WLF equation (Ferry [59]) is used to describe the time–temperature shift factor a_T:

$$\log_{10} a_T = -\frac{C_1(T - T_r)}{C_2 + (T - T_r)} \tag{22}$$

where C_1 and C_2 are constants and T_r is a reference temperature. The best way to apply the WLF equation is to determine the constants specially for each material by fitting the equation to experimental data. In the absence of relevant experimental data, a crude approximation is to use the so-called 'universal values' $C_1 = 17.44$, $C_2 = 51.6$ K and $T_r = T_g$.

For temperatures outside the above range or for semi-crystalline materials, an Arrhenius expression is chosen:

$$\ln a_T = \frac{E_a}{R}\left(\frac{1}{T} - \frac{1}{T_r}\right), \tag{23}$$

where E_a is the activation energy and R the gas constant. Materials obeying the time–temperature superposition principle are called thermorheologically simple materials. Thermorheological simplicity assumes that the isothermally determined viscoelastic functions remain substantially unchanged in shape as functions of the logarithmic time or frequency scales, so that the time–temperature superposition principle can be applied to describe the temperature dependence of the viscoelastic properties of the material. We have assumed that the composite exhibits thermorheological simple behaviour; this however should be regarded as a rough approximation. A number of exceptions to thermorheological simplicity have been reported (Plazek [60] and Dutta and Edward [61]). Several materials including non-fibre filled amorphous polymers actually exhibit thermorheological complex behaviour. Thermorheological complex polymers are not reducible by simple superposition principles. Dutta and Edward [61] have shown that using two or more activation energies in the Arrhenius equation for different relaxation mechanisms could better describe the temperature dependence of the relaxation functions for thermorheological complex materials, but the method will not be pursued here due to lack of experimental data.

The total stress tensor in Eq. (20) can be split into a hydrostatic pressure and a extra stress part:

$$\boldsymbol{\sigma} = -p_h \boldsymbol{I} + \boldsymbol{\tau} \tag{24}$$

where p_h is the hydrostatic pressure, $\boldsymbol{I}$ is the unit tensor and $\boldsymbol{\tau}$ is the extra stress tensor.

In the injection moulding situation the fibres are nearly aligned in the flow plane. We can take the fibre direction as the 1-direction and the local thickness direction as the 3-direction. The part is considered to be fully constrained within the 1–2 plane while it is in the mould. The hydrostatic pressure can then be written as

$$p_h = -\frac{1}{3}\sigma_{ii} = \int_0^t \left(\beta \frac{\partial T}{\partial t'} - K \operatorname{Tr} \dot{\varepsilon}\right) \mathrm{d}t', \tag{25}$$

where β and K are given in terms of the elastic and thermal properties in contracted notations

$$\beta = \tfrac{1}{3}\Big[\Big(c_{11}^{(e)} + c_{12}^{(e)} + c_{13}^{(e)}\Big)\alpha_1 + \Big(c_{12}^{(e)} + c_{22}^{(e)} + c_{23}^{(e)}\Big)\alpha_2 + \Big(c_{13}^{(e)} + c_{23}^{(e)} + c_{33}^{(e)}\Big)\alpha_3\Big], \tag{26}$$

$$K = \tfrac{1}{3}\Big(c_{13}^{(e)} + c_{23}^{(e)} + c_{33}^{(e)}\Big). \tag{27}$$

The components of the extra normal stress are given by

$$\tau_{11}(t) = 2\int_0^t G_1(\xi(t) - \xi(t'))\frac{\partial \varepsilon_{11}^{d}}{\partial t}\,dt' - \int_0^t \beta_1(\xi(t) - \xi(t'))\frac{\partial T}{\partial t}\,dt', \tag{28}$$

$$\tau_{22}(t) = 2\int_0^t G_2(\xi(t) - \xi(t'))\frac{\partial \varepsilon_{22}^{d}}{\partial t}\,dt' - \int_0^t \beta_2(\xi(t) - \xi(t'))\frac{\partial T}{\partial t}\,dt', \tag{29}$$

$$\tau_{33}(t) = 2\int_0^t G_3(\xi(t) - \xi(t'))\frac{\partial \varepsilon_{33}^{d}}{\partial t}\,dt' - \int_0^t \beta_3(\xi(t) - \xi(t'))\frac{\partial T}{\partial t}\,dt', \tag{30}$$

where ε_{ij}^{d} is the deviatoric strain defined as

$$\varepsilon_{ij}^{d} = \varepsilon_{ij} - \tfrac{1}{3}\mathrm{Tr}\,\varepsilon\,\delta_{ij}. \tag{31}$$

The G_i and β_i ($i = 1, 2, 3$) in the above equations are assumed to be

$$G_1(t) = G_1(0)F(t), \tag{32}$$

$$G_2(t) = G_2(0)F(t), \tag{33}$$

$$G_3(t) = G_3(0)F(t), \tag{34}$$

$$\beta_1(t) = \beta_1(0)F(t), \tag{35}$$

$$\beta_2(t) = \beta_2(0)F(t), \tag{36}$$

$$\beta_3(t) = \beta_3(0)F(t), \tag{37}$$

with

$$G_1(0) = \tfrac{1}{2}(c_{23}^{(e)} - 2c_{13}^{(e)} + c_{33}^{(e)}), \tag{38}$$

$$G_2(0) = \tfrac{1}{2}(c_{13}^{(e)} - 2c_{23}^{(e)} + c_{33}^{(e)}), \tag{39}$$

$$G_3(0) = \tfrac{1}{4}(2c_{33}^{(e)} - c_{23}^{(e)} - c_{13}^{(e)}), \tag{40}$$

$$\beta_1(0) = \tfrac{1}{3}\Big[(2c_{11}^{(e)} - c_{12}^{(e)} - c_{13}^{(e)})\alpha_1 + (2c_{12}^{(e)} - c_{22}^{(e)} - c_{23}^{(e)})\alpha_2 + (2c_{13}^{(e)} - c_{23}^{(e)} - c_{33}^{(e)})\alpha_3\Big], \tag{41}$$

$$\beta_2(0) = \tfrac{1}{3}\Big[(2c_{12}^{(e)} - c_{11}^{(e)} - c_{13}^{(e)})\alpha_1 + (2c_{22}^{(e)} - c_{12}^{(e)} - c_{23}^{(e)})\alpha_2 + (2c_{23}^{(e)} - c_{13}^{(e)} - c_{33}^{(e)})\alpha_3\Big], \tag{42}$$

$$\beta_3(0) = \tfrac{1}{3}\Big[(2c_{13}^{(e)} - c_{11}^{(e)} - c_{12}^{(e)})\alpha_1 + (2c_{23}^{(e)} - c_{12}^{(e)} - c_{22}^{(e)})\alpha_2 + (2c_{33}^{(e)} - c_{13}^{(e)} - c_{23}^{(e)})\alpha_3\Big], \tag{43}$$

where we have assumed that all $G_i(t)$ and $\beta_i(t)$ depend on the same relaxation function $F(t)$. We approximate the relaxation function as a sum of weighted exponential functions, i.e.,

$$F(t) = \sum_{k=1}^{N} g_k \exp\left(-\frac{t}{\lambda_k}\right), \tag{44}$$

in which $\sum_{k=1}^{N} g_k = 1$. To use this model, it is necessary to have a discrete relaxation spectrum, that is, a set of N pairs of values (g_k, λ_k).

Specially, for an isotropic material we have

$$c_{11}^{(e)} = c_{22}^{(e)} = \frac{2(1-\nu)}{1-2\nu} G \tag{45}$$

$$c_{12}^{(e)} = c_{13}^{(e)} = c_{23}^{(e)} = \frac{2\nu}{1-2\nu} G \tag{46}$$

where G is the shear modulus, and thus the anisotropic viscoelastic model reduces to an isotropic viscoelastic model like the ones used by Kabanemi and Crochet [16] and Baaijens [17]. It is also easy to show that the viscoelastic model reduces to the anisotropic elastic model by the correspondence principle [62], or by letting $\lambda \to \infty$.

3. Numerical methods

3.1. Numerical simulation of filling and packing

The governing Eq. (4) for determination of pressure in filling and packing phases are solved using a finite element method. The conventional Galerkin method is used to derive the finite element equations based on the local coordinate system, using a P^1–C^0 interpolation (For details see Kennedy [4]). A global/local coordinate transformation can be applied to model a three-dimensional geometry. The local coordinate system x_1, x_2, x_3 is such that x_1 and x_2 define the plane of the flow and x_3 indicates the thickness direction. It is most convenient to use three-node triangular elements to discretize the cavity and two-node beam elements to model runner systems.

For tracking the flow front, each triangular element is further divided into three sub-areas by linking the centroid of the element to the midpoint of its three edges. For each vertex node, the sum of all sub-areas containing that node defines a control volume. After solving for pressure, the flow rate into each node on the flow front can be calculated. Given a time step, the control volume associated with that node can be tested to see if it is full. Once the node is filled, the flow front is advanced by incorporating all nodes connected to the last node to fill into the flow front.

The transient heat transfer analysis for the polymer during filling and packing uses a finite difference method that requires a discretization of the time domain as well as a spatial discretization across the gapwise direction at each finite element. In any time step the convection and viscous dissipation terms from previous time step are treated as source terms. A cycle-averaged mould temperature at the metal-polymer interface is used as temperature boundary conditions. The cycle-averaged temperature of the metal mould surface can be efficiently obtained by solving a three-dimensional steady-state heat conduction equation using a boundary element method (e.g., Rezayat and Burton [63]). In real

situations, at the polymer/mould interface the temperature is normally higher at the polymer surface than at the mould surface due to the existence of a thermal contact resistance between the polymer and the mould. In the present paper, we assume that the polymer is in perfect contact with the mould and neglect the effect of the thermal contact resistance because of a lack of definitive data.

Most earlier numerical simulations of mould filling and packing assumed that the flow and temperature fields are symmetrical about the cavity mid-surface. The simplification allows calculations to be performed for one half of the cavity thickness, enabling both considerable gain in computational speed and reduction of storage requirements. However, in many practical situations the assumption is not valid. One may expect an asymmetrical flow in the case of asymmetrical mould cooling or in the case of bifurcation of mid-surface as shown by Couniot et al. [64] and Zoetelief et al. [65]. Warpage of the finished part may be sensitive to the asymmetry. In order to predict warpage accurately, we hence reject the symmetry assumption and calculate flow and temperature fields at all points through the thickness.

3.2. Prediction of fibre orientation

The evolution equation to be solved is Eq. (6), i.e., the anisotropic rotary diffusion equation. The interaction coefficient tensor corresponding to $a_R = 20$ and $nL^3 = 50$, is given in Appendix A. The eigenvalues of this tensor are 6.287×10^{-2}, 2.732×10^{-3} and 1.822×10^{-3}; the difference between the eigenvalues suggests that the use of the anisotropic version of the rotary diffusion equation is more appropriate.

The numerical method used for integrating the equation is based on the explicit Euler time–differencing scheme; the magnitude of the time step is smaller than that used for the flow front advancement analysis and is bounded by the Courant stability criterion:

$$\Delta t_f < \frac{\Delta x}{|v|}, \tag{47}$$

where Δx represents the size of an element and $|v|$ the norm of the velocity. For triangular elements Δx is the minimum of the distances from the centroid to each of the three vertices, and v is the flow speed at the mid-plane.

Solution of the evolution equations is an initial value problem. We begin with specifying the initial orientation tensor at elements connected to the gates. The exact inlet conditions of the fibre orientation are usually unknown. However, the initial orientation state specified at the inlet has been found to have little impact on the final orientation results. In order to explain this, let us consider the distance required for the fibres to reach the steady state in a shear flow. The average distance can be estimated by $0.5\,\gamma h$ where γ is the shear strain required for the fibres to reach the steady-state limit, and h is the gap width of the flow channel. It is found that γ is of the order 30 for a random initial orientation configuration (see Appendix A), indicating that the reorientation completes within a distance of 15 h. When the flow front is advanced more elements will be included in the flow domain. For an element that is just included in the flow domain, the initial fibre orientation is determined by convecting the orientation at neighbouring elements to the new element.

As mentioned, the Hele–Shaw approximation takes no account of the effect of the lateral wall on the flow field. This can also lead to errors in the prediction of fibre orientation within a boundary layer of order h where the ‘edge effect’ is actually non-negligible. Our experience showed that for some cases

the warpage of the part is sensitive to the fibre orientation along the edges, depending on the particulars of the part structure. Two ad-hoc treatments have been made to take into account the edge effect. The first is to impose a vanishing tangential velocity along the edge walls when computing velocity gradients from the velocity field for fibre orientation calculations. The second is to employ an 'infinite-aspect-ratio' assumption for those fibres close to the walls [37].

3.3. Calculation of thermally and pressure-induced stresses

3.3.1. Assumptions and boundary conditions

Assumptions: For simplifying the calculation of thermally and pressure induced stresses in the injection moulding process, the following assumptions are made:

1. With respect to the local coordinates in which the x_3-direction is normal to the local mid-plane, the shear strains $\varepsilon_{13} = \varepsilon_{23} = 0$.
2. The normal stress σ_{33} is constant across the thickness.
3. As long as $\sigma_{33} < 0$, the material sticks to the mould walls.
4. Before ejection, the part is fully constrained within the plane of the part such that the only non-zero component of strain is ε_{33}.
5. Mould elasticity is neglected.

Boundary Conditions: The following different cases are considered for the local boundary conditions in terms of the normal stress σ_{33}:

Case 1: If the part is in the mould and there is coexistence of a solid layer and liquid core, now the normal stress equals the opposite of the fluid pressure:

$$\sigma_{33} = -p. \tag{48}$$

All strain components except for ε_{33} are zero.

The change of a material point from liquid to solid is determined based on a critical temperature. The critical temperature is experimentally obtained from a differential scanning calorimeter (DSC) cooling trace. For amorphous materials this temperature is inferred as the temperature at which the material has completed the glass transition phase. For semi-crystalline materials, this temperature is inferred as the temperature at which the material has undergone most of the re-crystallization process.

Case 2: When the part is in the mould and the material has solidified throughout the thickness, the material may either stick to the mould walls or detach from the walls. If it still contacts the walls, then σ_{33} should be determined by the condition

$$\int_{-h/2}^{h/2} \varepsilon_{33}\, \mathrm{d}x_3 = 0, \tag{49}$$

otherwise $\sigma_{33} = 0$. All strain components are still zero except for ε_{33}.

Case 3: After the part is ejected, no outside loads or constraints are applied to the part, thus the boundary condition is that the surface traction equals zero:

$$\sigma_{ij} n_j = 0, \tag{50}$$

where n_i is the normal outward unit vector field on the boundary. The thermal stresses just before ejection form the initial stresses in the part. In addition, we need to impose a suitable set of support constraints to the structure to prevent the body from undergoing unlimited rigid body motion.

3.3.2. Discrete formulation

For the numerical solution of the thermal stress problem, the linear thermoviscoelastic equation is written in a temporally discrete form. In this way, the stress state at time t_{n+1} can be evaluated from the known stress state at time t_n. First we write Eq. (25) as

$$p_h(t_{n+1}) = p_h(t_n) + \beta\Delta T - K\,\mathrm{Tr}\Delta\,\varepsilon, \tag{51}$$

where ΔT and $\Delta\varepsilon$ are the change in T and ε, respectively, during time step $\Delta t = t_{n+1} - t_n$.

We now establish the discrete formulation of Eqs. (28)–(30). After substituting Eq. (32), Eq. (35) and Eq. (44) into Eq. (28), τ_{11} can be decomposed as

$$\tau_{11}(t) = \sum_{k=1}^{N}\left[s_{11}^{(k)}(t) - \Theta_1^{(k)}(t)\right], \tag{52}$$

where

$$s_{11}^{(k)}(t) = 2G_1(0)g_\mathrm{k}\int_0^t \exp\left(-\frac{\xi(t)-\xi(t')}{\lambda_\mathrm{k}}\right)\mathrm{d}\varepsilon_{11}^{\mathrm{d}}(t'), \tag{53}$$

$$\Theta_1^{(k)}(t) = \beta_1(0)g_\mathrm{k}\int_0^t \exp\left(-\frac{\xi(t)-\xi(t')}{\lambda_\mathrm{k}}\right)\mathrm{d}\varepsilon_{11}^{\mathrm{d}}(t'). \tag{54}$$

By differentiating Eq. (53) with respect to t, we obtain

$$\frac{\mathrm{d}s_{11}}{\mathrm{d}t} + \frac{1}{\lambda}\frac{\mathrm{d}\xi}{\mathrm{d}t}s_{11} = 2G_1(0)g_\mathrm{k}\frac{\mathrm{d}\varepsilon_{11}^{\mathrm{d}}}{\mathrm{d}t}. \tag{55}$$

The differential equation can then be discretized using a finite difference scheme which gives

$$\frac{s_{11}(t_{n+1}) - s_{11}(t_n)}{\Delta t} + \frac{1}{\lambda}\frac{\Delta\xi}{\Delta t}s_{11}(t_{n+1}) = 2G_1(0)g_k\frac{\Delta\varepsilon}{\Delta t}, \tag{56}$$

so that

$$s_{11}^{(k)}(t_{n+1}) = \zeta_\mathrm{k}\left[s_{11}^{(k)}(t_n) + 2G_1(0)g_\mathrm{k}\Delta\varepsilon_{11}^{d}\right] \tag{57}$$

where

$$\zeta_\mathrm{k} = \left(1 + \frac{\Delta\xi}{\lambda_\mathrm{k}}\right)^{-1} \tag{58}$$

and $\Delta\xi$ is approximated by

$$\Delta\xi = \frac{\Delta t}{a_\mathrm{T}} \tag{59}$$

Similarly, for Eq. (54), we obtain

$$\Theta_1^{(k)}(t_{n+1}) = \zeta_k[\Theta_1^{(k)}(t_n) + \beta_1(0)g_k\Delta T] \tag{60}$$

Thus we have established recurrence formulations for the calculation of τ_{11}. The same discretization procedure is applied to obtain recurrence formulations for τ_{22} and τ_{33}. Since the axes of the coordinate system are defined in the fibre principal directions (assuming that the fibres lie parallel to the mid-plane), the in-plane shear stress τ_{12} is zero. After we transform the coordinates to the local element system, we will generally have no-zero in-plane shear stress components.

We now consider the incremental strain. Assumption 4 implies

$$\mathrm{Tr}(\Delta\varepsilon) = \Delta\varepsilon_{33}, \tag{61}$$

$$\Delta\varepsilon_{11}^{\mathrm{d}} = \Delta\varepsilon_{22}^{\mathrm{d}} = -\tfrac{1}{3}\Delta\varepsilon_{33}, \tag{62}$$

$$\Delta\varepsilon_{33}^{\mathrm{d}} = \tfrac{2}{3}\Delta\varepsilon_{33}. \tag{63}$$

Since the stress σ_{33} is given as a boundary condition, the incremental strain component $\Delta\varepsilon_{33}$ at the time interval (t_n, t_{n+1}) can be calculated on the basis of $\sigma_{33}(t_{n+1})$ and the previous results at t_n. The stress component $\sigma_{33}(t_{n+1})$ can be expressed as

$$\sigma_{33}(t_{n+1}) = \sigma_{33}^* + \left(K + \frac{4}{3}G_3(0)\sum_{k=1}^{N}\zeta_k g_k\right)\Delta\varepsilon_{33}, \tag{64}$$

where σ_{33}^* is given by

$$\sigma_{33}^* = -\left\{p_h(t_n) + \beta\Delta T + \sum_{k=1}^{N}\zeta_k[\Theta_3^{(k)}(t_n) + \beta_3 g_k\Delta T]\right\} + \sum_{k=1}^{N}\zeta_k s_{33}^{(k)}(t_n). \tag{65}$$

Thus,

$$\Delta\varepsilon_{33} = \frac{\sigma_{33}(t_{n+1}) - \sigma_{33}^*}{K + \frac{4}{3}G_3(0)\sum_{k=1}^{N}\zeta_k g_k}. \tag{66}$$

Assuming that the results at time t_n are known, the computation procedure for time t_{n+1} is summarized as follows:

1. Calculate the pressure, velocity, temperature and fibre orientation fields at t_{n+1} and calculate $\Delta T = T(t_{n+1}) - T(t_n)$.
2. Calculate thermo-mechanical properties using the newly obtained fibre orientation tensors.
3. Calculate the time–temperature shift factor a_T, the pseudo-time step $\Delta\xi$ and ζ_k ($k = 1,2,\ldots,N$) based on Eqs. (22) and (23), Eqs. (58) and (59). In Eq. (59) a_T is the average value of the a_T's taken at the old and the new temperatures.
4. Determine σ_{33} by identifying whether a molten core still exists.
5. Calculate σ_{33}^* and $\Delta\varepsilon_{33}$ based on Eqs. (65) and (66), respectively.
6. Calculate p_h, τ_{11}, τ_{22} and τ_{33} using Eqs. (51) and (52), etc.
7. Calculate σ_{11} and σ_{22} based on Eq. (24).

The calculation is performed element by element at each layer.

3.4. Structural analysis

As long as the part is constrained by the mould, no calculation of the displacements is required. After ejection (the free quench case), however, the displacement field is solved using a finite element method. The finite element analysis uses three-node triangular elements with 18 degrees of freedom for each element (six at each node). This type of element allows us to use the same finite element meshes as used in filling and packing simulations. The element is constructed by superimposing the local membrane formulation due to Bergan and Nygård [66] and Bergan and Felippa [67] with the linear bending formulation due to Batoz and Lardeur [68]. The material properties can vary from one element to another. Within the restriction that the material properties are not strongly asymmetric about the mid-surface, it is also possible to include variations of the mechanical properties across the thickness. At each point there are two orthogonal directions with respect to which the elastic moduli take on principal values. The directions are associated with the final state of the fibre orientation.

The calculated thermally and pressure induced stresses serve as the initial stresses to form the load term in the finite element equations. Once the load and boundary conditions are applied, the unknown nodal displacements can be calculated to determine the final size and the deformed shape of the part.

Although in the finite element structural analysis of the freely quenched part we can continue the thermoviscoelastic approach, the analysis could be very time-consuming. An alternative approach is to assume an elastic solid behaviour for the material upon ejection and to perform one more step of in-mould thermal stress calculation in which the material is forced to cool down from the ejection temperature to the ambient temperature. It is then possible to use an isothermal elastic analysis to calculate the deformation of the part after ejection.

The finite element method has been implemented for small deflection, large deflection and buckling analyses. If the resulting change in geometry does not significantly alter the stiffness of the structure, the small deflection analysis would be adequate. However experience shows that loading can be high enough to cause buckling of the component.

4. Results and discussion

This section presents numerical results of thermally and pressure induced stresses, shrinkage and warpage for the case of fibres with $a_R = 20$ and $\phi = 0.1$ ($nL^3 = 50$). The interaction coefficient tensor and details of material parameters used in the calculation are given in Appendix A and Appendix B, respectively.

4.1. Example 1

In this example, simulations are performed for a fan-gated rectangular part 200 mm long, 40 mm wide and 2 mm thick, as shown in Fig. 1. The mould was previously used by Thomas and McCaffrey [69] for an experimental study on shrinkage. The geometry of the cavity permits the fibres to align themselves mainly in the length direction of the part, and so allows the shrinkage parallel and perpendicular to the fibre direction to be examined.

The simulations have been performed with varying packing pressure ranging from 30 MPa to 110 MPa; in all cases the packing time is 15 s and the cooling time is 20 s. Melt temperature is assumed

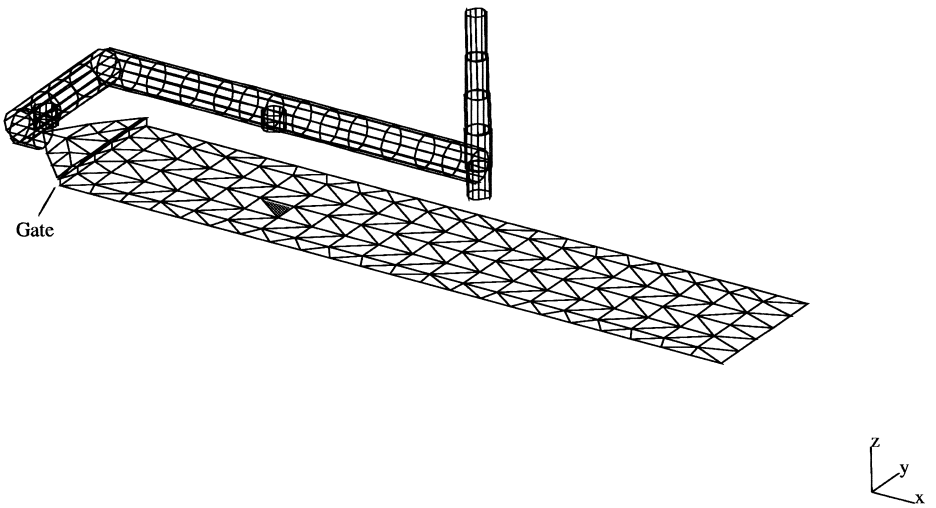

Fig. 1. Fan-gated rectangular part and the finite element mesh. The shaded element shows the position where the results are plotted in Figs. 2 and 3.

to be 240°C. Mould temperature is 60°C applied to both top and bottom sides of the cavity, and the injection rate is chosen to be 36 $cm^3\ s^{-1}$.

In order to show the effects of pressure and solidification history on the thermally and pressure induced stresses, we choose a typical element located at about 1/3 of the flow path downstream from the gate and in the centre of the strip (the element is shaded in Fig. 1) to display the predicted pressure history and the growth of the frozen layer (Fig. 2). The corresponding packing pressure applied at the nozzle is 110 MPa. The filling stage ends at $t = 0.86$ s. During filling the pressure changes from 0 to

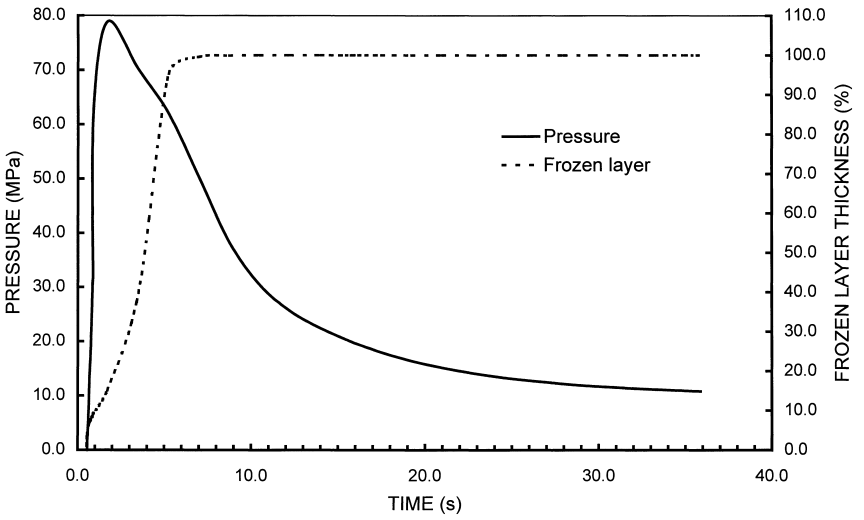

Fig. 2. Predicted cavity pressure and frozen layer as function of time for an element a quarter way of the flowpath as shown in Fig. 1.

about 30 MPa, and a very thin frozen layer (within 8.5% of the half thickness) develops under the relatively low pressure. As the packing stage starts, the pressure continues to increase and quickly reaches the highest level (>75 MPa) when $t = 1.5 – 2.0$ s, and at the same time the frozen layer grows further inward. The material at the position about 10% – 20% of the half thickness from the wall freezes at the high pressure. Then the pressure slowly decays as the frozen layer grows toward the core region.

The gapwise in-plane stress profiles at successive times are plotted in Fig. 3(a) and (b) for σ_{11} and σ_{22}, respectively. We choose five typical time instants to display the results. They are (i) $t = 0.56$ s when the element has just been filled; (ii) $t = 0.86$ s at the end of the filling stage; (iii) $t = 1.68$ s when

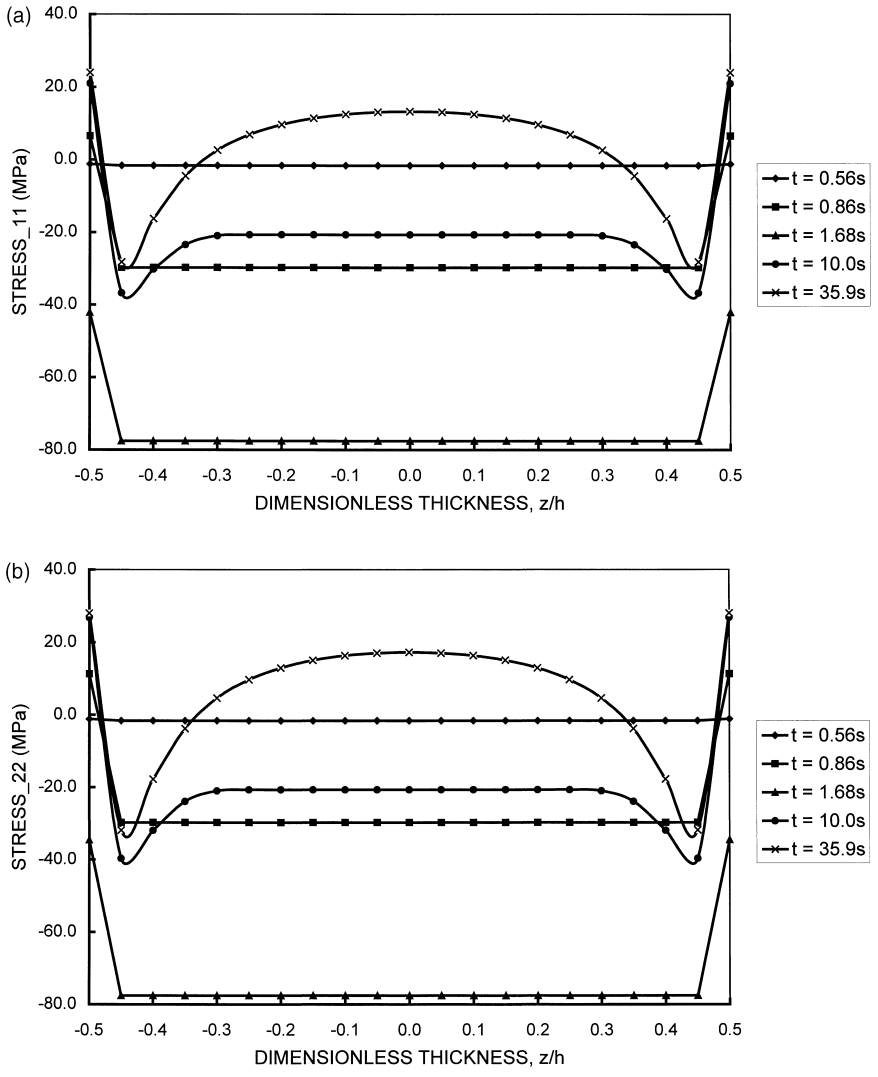

Fig. 3. Gapwise thermally and pressure induced stress profiles at successive times. (a) σ_{11} at different times; (b) σ_{22} at different times; (c) comparison of σ_{11} and σ_{22} at $t = 35.9$ s.

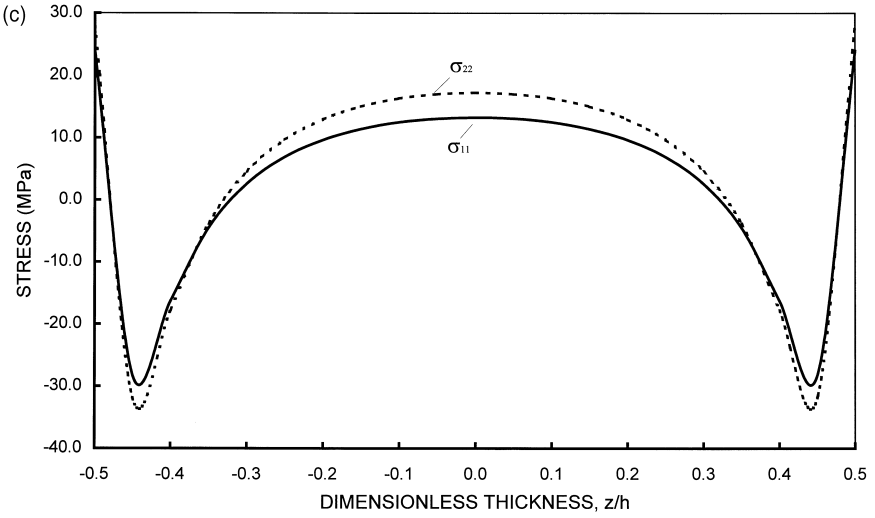

Fig. 3. (*Continued*)

the pressure reaches its peak value; (iv) $t = 10.0$ s after the core is frozen; and (v) $t = 35.9$ s just before ejection. As can be seen, before complete solidification the stresses in the molten core equal the negative of the fluid pressure, while the stresses in the frozen skin layer increase as consequence of the constrained cooling. After complete solidification the stresses throughout the whole thickness increase due to the decrease in both pressure and temperature. The final profile at the time $t = 35.9$ s shows that considerable tensile stresses have been built up in the surface layer, followed by a sharp decline in the region more inward (compressive in our case), then increase and become tensile again in the core. Clearly, the existence of the relatively high tensile stresses in the skin and core regions is associated with the relatively low pressure under which the skin and the core have frozen, while the existence of the minima in the intermediate region is due to the fact that the material in this region has frozen at the maximum pressure. This pattern of stress profile is typical for injection moulded parts, though exceptions indeed exist.

Baaijens [17] and other authors, as mentioned earlier, solved for thermal residual stresses using an isotropic material assumption. Although the general patterns of the stress profiles they predicted are quite similar to our predictions, their models essentially predict equal stress components σ_{11} and σ_{22}, while in our predictions the two components are significantly different. The differences are caused by the anisotropy in thermal expansion coefficient, Young's modulus and Poisson ratios, in combination with the relaxation effect. Fig. 3(c) compares the final stress profiles of σ_{11} and σ_{22} (at $t = 35.9$ s), showing that σ_{22} has higher tensile stresses at both the surface and the core, and a higher absolute value of the compressive stresses as well. The trend, however, is case-dependent rather than a rule.

Fig. 4 shows the predicted pressure history at different locations along the flow path, including the pressure profiles at the nozzle, near the gate, halfway down to the end, and near the end of the flow path. Fig. 5(a) and (b) show the stress distribution of σ_{11} and σ_{22}, respectively, along the mould length at the time $t = 35.9$ s. The surface tensile stresses near the gate are higher than at the locations away from the gate, related to the higher peak pressure near the gate.

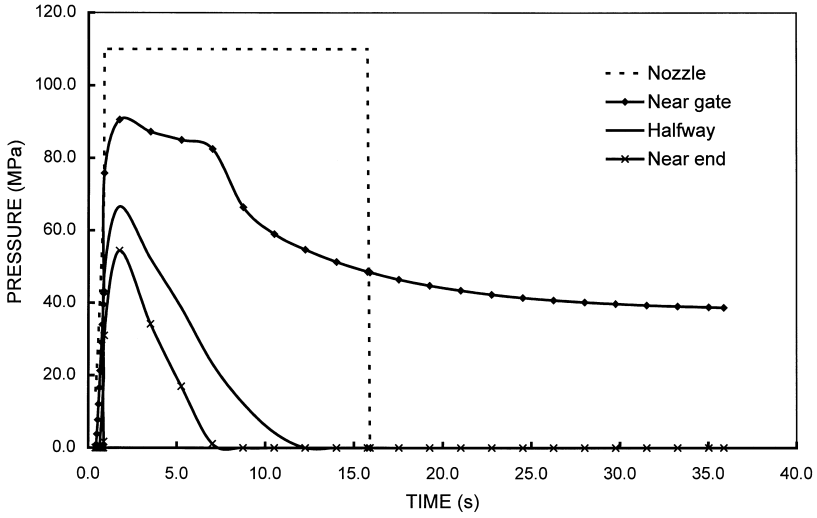

Fig. 4. Predicted cavity pressure at different locations along flow path.

We now examine the shrinkage results. Fig. 6 defines lines AB and CD on which the linear shrinkage values are measured. Fig. 7 compares the computed and experimental measured shrinkage data at different packing pressure conditions, where X-SHRK denotes the linear shrinkage in the length direction on line AB, and the Y-SHRK denotes the linear shrinkage in the width direction on line CD. The results show a reasonable agreement. Both computed and experimental data show that shrinkage decreases with increasing packing pressure. This is because higher pressure introduces lower tensile residual stresses. One also sees that the shrinkage values in the length direction are much smaller than those in the width direction at the same pressure. The reason for this behaviour is that the alignment of fibres has afforded higher stiffness and lower thermal expansion coefficient in the length direction of the part.

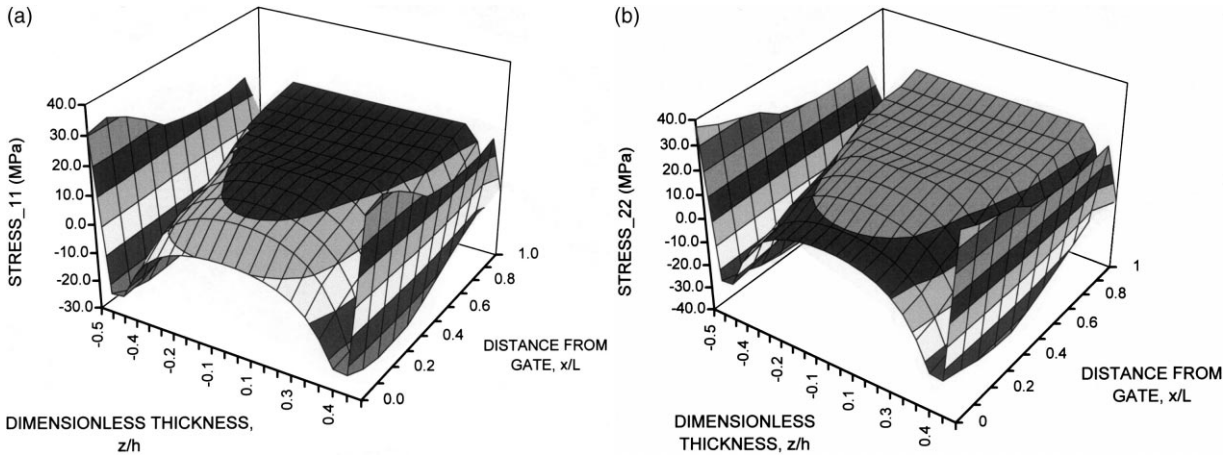

Fig. 5. Stress distribution along the mould length. In the length direction axis: (a) σ_{11} (b) σ_{22}.

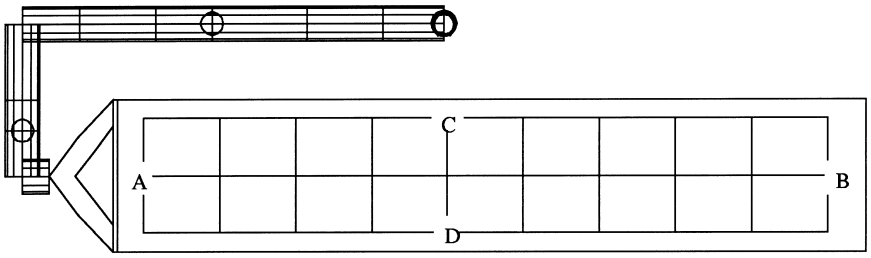

Fig. 6. Definition of lines AB and CD on which shrinkage data are measured.

4.2. Example 2

This example considers a thin plate (100 mm × 100 mm × 1.5 mm) with a thick rib (100 mm × 10 mm × 3 mm). It is representative of geometries where warpage can result from differential in-plane shrinkage in different regions of the part, even if the mould temperature is uniform on both sides. The melt temperature used in the calculation is 240°C, mould temperature is 60°C applied on both sides of the mould, injection rate is 16 $cm^3\ s^{-1}$, packing pressure is 60 MPa, packing time is 15 s and cooling time is 10 s.

Fig. 8 shows the shape of the part, the position of the injection node and the predicted fibre orientation distribution. Here the orientation distribution is graphically represented by ellipses. The axes of these ellipses adopt the direction and the length of the eigenvectors and the eigenvalues of the calculated orientation tensors a_{ij}, respectively. The major axis indicates the direction of preferred fibre orientation, while the roundness of the ellipse is a measure of the degree of alignment. That is, a circle

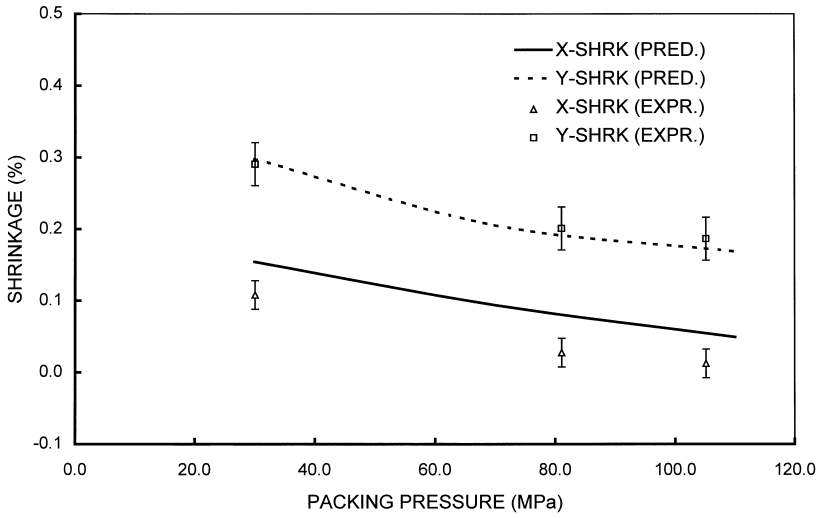

Fig. 7. Comparison of predicted and experimental shrinkage at different levels of packing pressure. The shrinkage data X-SHRK and Y-SHRK shown are measured, respectively on lines AB and CD as defined in Fig. 5.

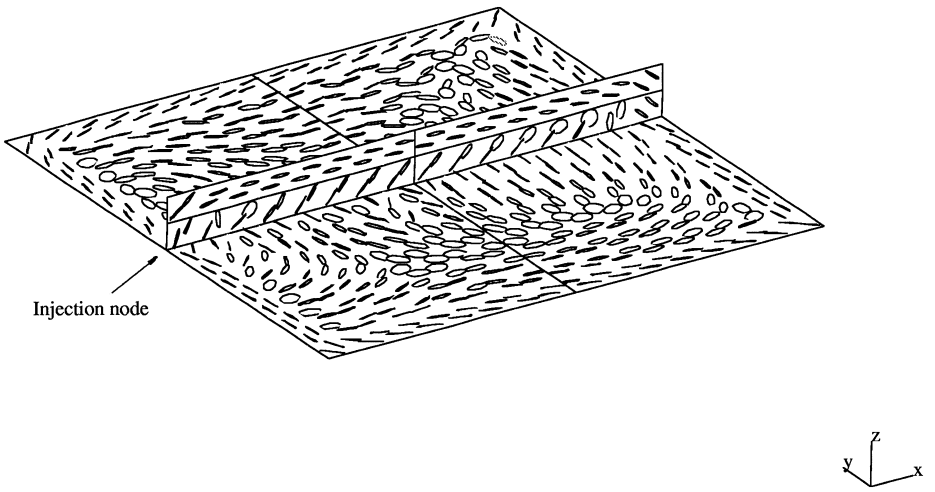

Fig. 8. Predicted flow-induced fibre orientation state in the part which is characterized by a thin flat plate with a thicker rib.

represents a random orientation, whereas a sharp line represents a near-full alignment. The fibre orientation distribution varies from layer to layer. What we display here is the average orientation obtained by averaging the orientation tensor through the thickness.

In order to examine the effect of the orientation on warpage, we first use the isotropic thermoviscoelastic model to analyse this problem without considering the fibre orientation. The result shows that the part after ejection becomes slightly concave towards the rib side (Fig. 9(a)). This is common in the case of isotropic material. In general, the cooling rate of the thick rib is lower than that of the thin plate. Consequently the rib shrinks more than the flat-plate section, thus causing the part to warp as shown.

We then use the anisotropic thermoviscoelastic model. The warped part is found to be convex towards the rib side as shown in Fig. 9(b). The fibre orientation distribution can explain why the opposite direction of warpage occurs. As previously shown in Fig. 8, the fibres in the rib region are highly aligned along the rib direction, whereas the fibres are seen to be more randomly distributed over the flat plate and as a result the anisotropy is less severe in the plate section. Since the thermal expansion coefficient is low and the stiffness is high in the fibre direction, the rib will shrink less in its length direction and this causes the part to bend towards the plate side. The opposite trends of warpage due to the existence of fibres do occur in many (although not all) of our case studies, both numerical and experimental. This example addresses further the necessity to use anisotropic models for fibre-reinforced materials.

4.3. Example 3

Finally we compute warpage in a complex part shown in Fig. 10 which is characterized by a box-like shape with seven gates. Its length and width is about 248 mm and 130 mm, respectively. The thickness in most areas is 2.5 mm.

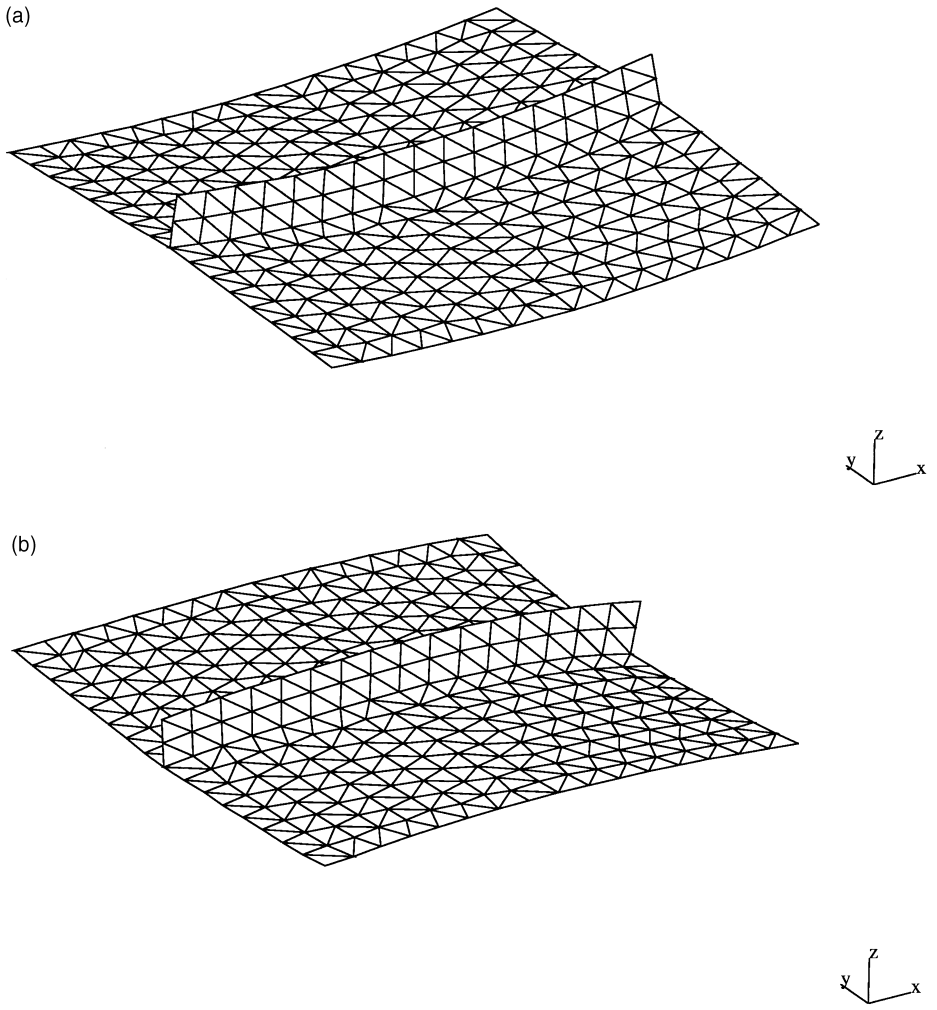

Fig. 9. (a) Warpage prediction based on isotropic material assumption. The deformed shape is concave towards the rib side. (b) Warpage prediction using anisotropic material model. The deformed shape is convex towards the rib side.

The melt temperature is 250°C, mould temperature is 65°C on both sides of the mould, injection rate is 80 $cm^3\ s^{-1}$, packing pressure is 58 MPa, packing time and cooling time are 3 and 5 s, respectively.

Fig. 10 also shows the predicted fibre orientation distributions in the part. The orientation distribution is quite complex, but one can see a pattern of concentric circles around the gates, and parallel alignment along edges and side walls. The holes also cause reorientation. Such fibre orientation distributions have significant effect on warpage as shown in Fig. 11. The largest warpage takes place in the front side wall in the z-direction. The maximum deflection in z-direction along the top edge of the front side wall is predicted to be 0.7 mm.

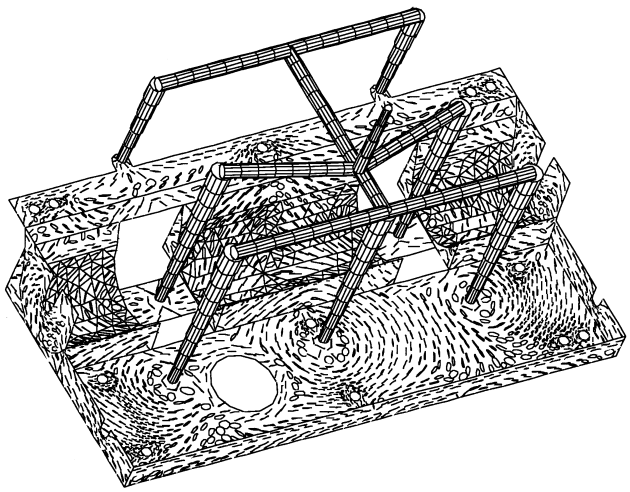

Fig. 10. The geometry of the seven point-gated box-like part and the predicted fibre orientation state.

5. Conclusions

The paper has described a numerical method for the prediction of residual stresses, shrinkage and warpage in injection moulded fibre-reinforced thermoplastics. Effects of pressure and thermal history, fibre orientation state and stress relaxation are taken into account through the simulation of the filling, packing and cooling stages of the injection moulding process. The final dimension and shape of the part after ejection are calculated by a finite element structural analysis. An anisotropic linear thermoviscoelastic material model is employed to describe the constitutive behaviour of the material.

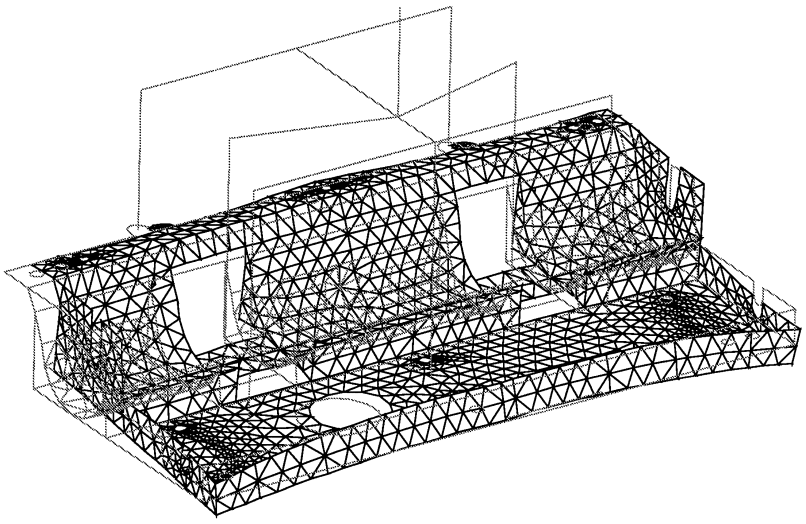

Fig. 11. Predicted final part dimension and shape compared with the original dimension and shape. Displacements are amplified by a factor of ten.

Material functions involved in this model are obtained using the predicted fibre orientation distributions and micromechanical theories. An anisotropic version of the Folgar–Tucker rotary diffusive equation has been proposed and applied for the calculation of flow-induced fibre orientation distribution.

The numerical examples indicate that the present method can be used to predict, at least semi-quantitatively, the shrinkage and warpage of the finished injection moulded parts with complex three-dimensional geometry.

The present work is limited by the use of the simple time-temperature superposition principle in the constitutive model to describe the temperature dependence, based on the assumed thermorheological simplicity. It would be desirable to have a model capable of describing thermorheological complex behaviour, especially for semi-crystalline materials. Some models have been investigated (e.g., [61]) but certainly need further development before being applied. Similarly, it would be possible to improve the predictive capability of the present method by including factors such as the mould elasticity and the wall slip if accurate experimental data were available for the determination of relevant properties.

Acknowledgements

This research is supported by an Australian Research Council Collaborative Grant (between Moldflow Pty. Ltd. and the University of Sydney). Material properties and experimental shrinkage data were provided by Moldflow's Centre for Polymer Testing and Research. The authors would like to thank Prof. C.L. Tucker III at University of Illinois at Urbana-Champaign for some useful discussions and for providing a computer program for the orthotropic closure approximation. Thanks are also due to Daicel Chemical Industries Ltd. for giving permission to use its designed component as a model part for our simulations. In addition, X-J. Fan wishes to acknowledge the support from the National Science Foundation of China.

Appendix A

A. Transient behaviour of fibre orientation in simple shear flow

The anisotropic tensor of the interaction coefficient corresponding to $a_R = 20$ and $nL^3 = 50$ predicted by the direct simulation is

$$\boldsymbol{C} = \begin{pmatrix} 6.28 \times 10^{-2} & 7.61 \times 10^{-4} & 1.86 \times 10^{-3} \\ 7.61 \times 10^{-4} & 2.74 \times 10^{-3} & 6.00 \times 10^{-5} \\ 1.86 \times 10^{-3} & 6.00 \times 10^{-5} & 1.88 \times 10^{-3} \end{pmatrix}. \tag{A1}$$

The components of the tensor, C_{ij} $(i, j = 1, 2, 3)$, are defined in the coordinate system with the 1-axis in the flow direction, the 3-axis in the velocity gradient direction, and the 2-axis in the neutral direction.

Fig. 12 shows the transient behaviour of the orientation components in a simple shear flow $(v_1 = \dot{\gamma}x_3,\ v_2 = 0,\ v_3 = 0)$, calculated using the above interaction coefficient tensor with the orthotropic closure approximation. It would be interesting to find a corresponding isotropic C_I with which the the steady-state a_{11} predicted by the Folgar–Tucker isotropic diffusion model (using the same closure approximation) matches the corresponding result of the new anisotropic diffusion model. After some numerical experiments, the corresponding value is found to be $C_I = 0.0008$, considerably smaller

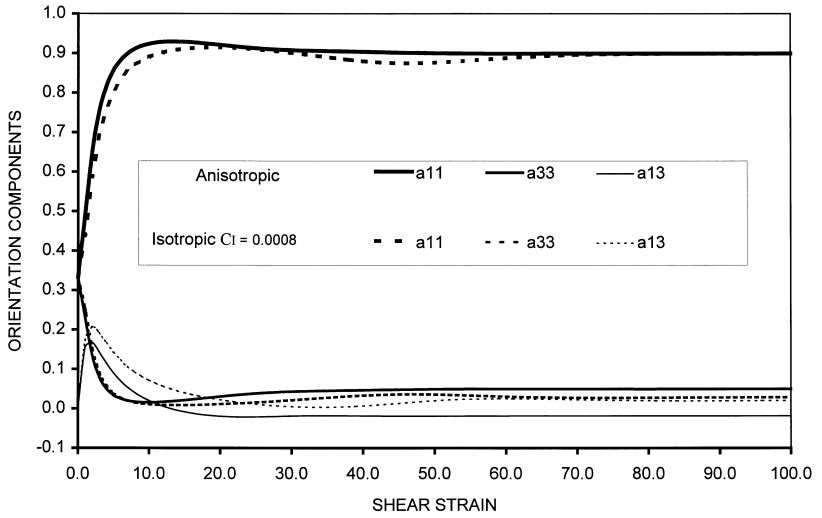

Fig. 12. Transient behaviour of fibre orientation components in simple shear flow ($v_1 = \dot{\gamma}x_3$, $v_2 = v_3 = 0$), predicted using the anisotropic rotary diffusion model (the solid lines) and an isotropic $C_I = 0.0008$ (the broken lines), both using the orthotropic closure approximation.

than the average value (Tr **C**)/3 = 0.0225. The orientation components obtained from $C_I = 0.0008$ are also plotted in the same graph for a comparison. One can see that the anisotropic diffusion model predicts a lower value of a_{13} and a slightly higher value of a_{33} as compared to the corresponding steady-state orientation components obtained using $C_I = 0.0008$.

In injection moulding flow simulations we use local element coordinate system. The velocity v at each element is not necessarily in the local element axis x_1 direction, thus the following transformation is needed

$$\boldsymbol{C}_{(\text{new})} = \boldsymbol{Q}^{\mathrm{T}}\boldsymbol{C}\boldsymbol{Q}, \tag{A2}$$

where

$$\boldsymbol{Q} = \begin{pmatrix} \cos\theta & \sin\theta & 0 \\ -\sin\theta & \cos\theta & 0 \\ 0 & 0 & 1 \end{pmatrix}, \tag{A3}$$

with

$$\theta = \tan^{-1}\left(\frac{v_2}{v_1}\right).$$

Appendix B

B. Material Parameters

The material characterized for the numerical simulation is an acrylonitrile-butadiene-styrene (STYLAC ABS R240A 20% (by weight) glass-fibre filled).

Table 2
Parameters in cross model

Parameter	Value
B (Pa s)	1.01×10^{-8}
T_b (K)	1.339×10^{4}
β (Pa^{-1})	5.670×10^{-8}
τ^* (Pa)	7.879×10^{4}
n	0.166

B.1. Viscosity

Viscosity testing was performed on a BOY15 injection moulding machine fitted with a slit die. The viscosity is modeled by the Cross model:

$$\eta = \frac{\eta_0}{1 + (\eta_0 \dot{\gamma}/\tau^*)^{(1-n)}}, \tag{B1}$$

where

$$\eta_0 = B \exp(T_b/T) \exp(\beta p)$$

provides temperature and pressure dependence.

The parameters are listed in Table 2.

B.2. Thermal properties

The thermal conductivity $k = 0.14\ \mathrm{W\ mK^{-1}}$ is taken as a constant value for both the melt and the solid phase. The value was measured using a Moldflow designed TC-200 thermal conductivity apparatus, based on measuring the heat flow and the temperature gradient across a known thickness and area of the polymer sample. The specific heat capacity is also taken as a constant value $c_p = 1773\ \mathrm{J\ kg^{-1}\ K^{-1}}$) for both the melt and the solid phase. The glass transition temperature at

Table 3
Parameters in P–V–T model

Coefficient	Lower temperature region	Upper temperature region
A_1	4.85×10^{6}	5.92×10^{6}
A_2	16.8	81.2
A_3	6.51×10^{7}	1.42×10^{8}
A_4	5.70×10^{9}	7.21×10^{9}
A_5	0	
A_6	0	
A_7	0	

$b_1 = -4.35 \times 10^{8}$.
$b_2 = -4.61 \times 10^{6}$.

Table 4
Elastic properties of polymer and fibre

Property	Value
Tensile modulus of fibre	72000 MPa
Tensile modulus of polymer	2300 MPa
Poisson ratio of filler	0.2
Poisson ratio of polymer	0.38
Average fiber length	0.2 mm
Average fiber diameter	0.01 mm
Fiber volume fraction	0.1

zero pressure is $T_g = 367.5$ K. The specific heat capacity and glass transition temperature are measured from the DSC tests.

B.3. P–V–T data

The quasi-equilibrium P–V–T behaviour is modeled using a seven-coefficient empirical model:

$$\hat{V} = \frac{A_1}{A_4 + p} + \frac{A_2 T}{A_3 + p} + A_5 \exp(A_6 T - A_7 p) \tag{B2}$$

which in fact has a total of eleven coefficients since the equation is broken into two regions: (i) the lower temperature region which describes the solid phase of the material and the solid-melt transition behaviour, and (ii) the upper temperature region which describes the material melt phase behaviour. Although the form of the equation is the same for the two regions, the corresponding coefficients take different values (in the upper temperature region A_5, A_6 and A_7 are always set to zero, so we need all together 11 coefficients instead of 14). Another equation is also needed to describe the boundary between the two temperature regions, which is given by

$$p = b_1 + b_2 T \tag{B3}$$

The parameters are listed in Table 3. These parameters were calculated by a least squares fit of the above model to the data measured using a Gnomix PVT Apparatus.

Table 5
Relaxation spectrum data

k	λ_k	g_k
1	1.0000×10^{-6}	9.8884×10^{-2}
2	8.3260×10^{-4}	4.2487×10^{-1}
3	6.9310×10^{-1}	4.7554×10^{-1}
4	5.7708×10^{2}	7.2610×10^{-5}
5	4.8040×10^{5}	5.0610×10^{-4}
6	4.0000×10^{8}	1.3450×10^{-4}

B.4. Component's elastic properties

The elastic properties for each component of the composite and fibre geometry provided by the material supplier are listed in Table 4. The fibre length and diameter are the statistical number average values. No information on the fibre length distribution is available.

B.5. Relaxation spectrum data

The relaxation spectrum data, obtained from dynamic shear experiments, are given in Table 5.

References

[1] M.R. Kamal, S. Kenig, The injection moulding of thermoplastics Part I. Theoretical model, Polym. Eng. Sci. 12 (1972) 294–301.
[2] C.A. Hieber, S.F. Shen, A finite-element/finite-difference simulation of the injection-moulding filling process, J. Non-Newtonian Fluid Mech. 7 (1980) 1–32.
[3] H.H. Chiang, C.A. Hieber, K.K. Wang, A unified simulation of the filling and postfilling stages in injection moulding Part 1. Formulation, Polym. Eng. Sci. 31 (1991) 116–124.
[4] P. Kennedy, Flow Analysis of Injection Molds, Hanser, Munich, 1995.
[5] M.J. Crochet, F. Dupret, V. Verleye, in: S.G. Advani (Ed.), Flow and Rheology in Polymer Composites Manufacturing, Elsevier, Amsterdam, 1994, Ch. 11.
[6] C.v.L. Kietzmann, J.P. Van Der Walt, Y.S. Morsi, A Free-front tracking algorithm for a control-volume Hele–Shaw method, Int. J. Num. Meth. Eng. 41 (1998) 253–269.
[7] R.C. Givler, M.J. Crochet, R.B. Pipes, Numerical predictions of fibre orientation in dilute suspensions, J. Compos. Mater. 17 (1983) 330–343.
[8] M.R. Kamal, S.K. Goyal, E. Chu, Simulation of injection mould filling of viscoelastic polymers with fountain flow, AIChE J. 34 (1988) 94–106.
[9] D.J. Coyle, J.W. Blake, C.W. Macosko, The kinematics of fountain flow in mould-filling, AIChE J. 33 (1987) 1168–1177.
[10] H. Mavridis, A.M. Vlachopoulos, The effect of fountain flow on molecular orientation in injection moulding, J. Rheol. 32 (1988) 639–663.
[11] R. Zheng, N. Phan-Thien, R.I. Tanner, Modelling the flow of a suspension fluid in injection moulding, in: Y.L. Yeow, P.H.T. Uhlherr (Eds.), Proc. 5th National Society of Rheology, Melbourne, 1990, pp. 141–144.
[12] D. Fauchon, H.H. Dannelongue, P.A. Tanguy, Numerical simulation of the advancing front in injection moulding, Int. Polym. Process. 6 (1991) 13–18.
[13] R.S. Bay, C.L. Tucker III, Fibre orientation in simple injection moldings Part 1. Theory and numerical methods, Polym. Compos. 13 (1992) 317–321.
[14] M. Gupta, K.K. Wang, Fibre orientation and mechanical properties of short-fibre-reinforced injection-moulded composites: simulation and experimental results, Polym. Compos. 14 (1993) 367–381.
[15] S.F. Walsh, Shrinkage and warpage prediction for injection moulded components, J. Reinforced Plas. Compos. 12 (1993) 769–777.
[16] K.K. Kabanemi, M.J. Crochet, Thermoviscoelastic calculation of residual stresses and residual shapes of injection moulded parts, Int. Polym. Process. 7 (1992) 60–70.
[17] F.P.T. Baaijens, Calculation of residual stress in injection moulded products, Rheol. Acta 30 (1991) 284–299.
[18] K.M.B. Jansen, Residual stresses in quenched and injection moulded products, Int. Polym. Process. 9 (1994) 82–89.
[19] F. Boitout, J.F. Agassant, M. Vincent, Elastic calculation of residual stresses in injection moulding: influence of mould deformation and pressure in the liquid, Int. Polym. Process. 10 (1995) 237–242.
[20] G. Titomanlio, K.M.B. Jansen, In-mould shrinkage and stress prediction in injection moulding, Polym. Eng. Sci. 36 (1996) 2041–2049.

[21] W.F. Zoetelief, L.F.A. Douven, A.J. Ingen-Housz, Residual thermal stresses in injection moulded products, Polym. Eng. Sci. 36 (1996) 1886–1896.
[22] L. Caspers, VIp, An Integral Approach to the Simulation of Injection Moulding, Ph.D. Thesis, Eindhoven University of Technology, 1996.
[23] W.C. Bushko, V.K. Stokes, Solidification of thermoviscoelastic melts Part 1. Formulation of model problem, Polym. Eng. Sci. 35 (1995) 351–364.
[24] W.C. Bushko, V.K. Stokes, Solidification of thermoviscoelastic melts Part 2. Effects of processing conditions on shrinkage and residual stresses, Polym. Eng. Sci. 35 (1996) 365–383.
[25] W.C. Bushko, V.K. Stokes, Solidification of thermoviscoelastic melts. Part 3. Effects of mould surface temperature differences on warpage and residual stresses, Polym. Eng. Sci. 36 (1996) 322–335.
[26] W.C. Bushko, V.K. Stokes, Solidification of thermoviscoelastic melts. Part 4. Effects of boundary conditions on shrinkage and residual stresses, Polym. Eng. Sci. 36 (1996) 658–675.
[27] S.G. Advani (Ed.), Flow and Rheology in Polymer Composite Manufacturing, Elsevier, Amsterdam, 1994.
[28] T.D. Papathanasiou, D.C. Guell (Eds.), Flow-induced Alignment in Composite Materials, Woodhead, Cambridge, UK, 1997.
[29] R. Zheng, N. McCaffrey, K. Winch, H. Yu, P. Kennedy, Predicting warpage of injection moulded fibre-reinforced plastics, J. Thermoplastic Compos. Mater. 9 (1996) 90–106.
[30] T.A. Osswald, S.-C. Tseng, Compression molding, in: S.G. Advani (Ed.), Flow and Rheology in Polymer Composites Manufacturing, Elsevier, Amsterdam, 1994, Ch. 10.
[31] M. Rezayat, R.O. Stafford, A Thermoviscoelastic model for residual stress in injection moulded thermoplastics, Polym. Eng. Sci. 31 (1991) 393–398.
[32] F.P. Folgar, C.L. Tucker, Orientation behaviour of fibres in concentrated suspensions, J. Reinforced Plastics and Compos. 3 (1984) 98–119.
[33] X.J. Fan, N. Phan-Thien, R. Zheng, A direct simulation of fibre suspensions, J. Non-Newtonian Fluid Mech. 74 (1998) 113–136.
[34] N. Phan-Thien, R. Zheng, Macroscopic modelling of the evolution of fibre orientation during flow, in: T.D. Papathanasiou, D.C. Guell (Eds.), Flow-Induced Alignment in Composite Materials, Woodhead, Cambridge UK, 1997. Ch. 3.
[35] G.B. Jeffery, The motion of ellipsoidal particles immersed in viscous fluid, Proc. Roy. Soc. Lond. A 102 (1922) 161–179.
[36] Y. Yamane, Y. Kaneda, M. Doi, Numerical simulation of semi-dilute suspensions of rodlike particles in shear flow, J. Non-Newtonian Fluid Mech. 54 (1994) 405–421.
[37] G.G. Lipscomb II, M.M. Denn, D.U. Hur, D.V. Boger, The flow of fibre suspensions in complex geometry, J. Non-Newtonian Fluid Mech. 26 (1988) 297–325.
[38] J. Rosenberg, M.M. Denn, R. Keunings, Simulation of non-recirculating flows of dilute fibre suspensions, J. Non-Newtonian Fluid Mech. 37 (1990) 317–345.
[39] R. Zheng, Boundary Element Methods for some Problems in Fluid Mechanics and Rheology, Ph.D. Thesis, University of Sydney, 1991.
[40] N. Phan-Thien, R. Zheng, A.L. Graham, The flow of a model suspension fluid past a sphere, J. Statist. Phys. 62 (1991) 1173–1195.
[41] N. Phan-Thien, A.L. Graham, A new constitutive model for fibre suspensions: flow past a sphere, J. Rheol. 30 (1991) 44–57.
[42] M.C. Altan, S.I. Güceri, R.B. Pipes, Anisotropic channel flow of fibre suspensions, J. Non-Newtonian Fluid Mech. 14 (1992) 65–83.
[43] C.L. Tucker III, Flow regimes for fibre suspensions in narrow gaps, J. Non-Newtonian Fluid Mech. 39 (1991) 239–268.
[44] D. Guell, M. Lovalenti, An examination of assumptions underlying the state of the art in injection moulding modeling, SPE ANTEC, 95 1 (1995) 728–732.
[45] S.G. Advani, C.L. Tucker III, The use of tensors to describe and predict fibre orientation in short fibre composites, J. Rheol. 31 (1987) 751–784.
[46] M. Doi, Molecular dynamics and rheological properties of concentrated solutions of rodlike polymers in isotropic and liquid crystalline phases, J. Polym. Sci. Polym. Phys. Ed. 19 (1981) 229–243.
[47] K. Nakamuta, T. Watanabe, K. Katayama, Some aspects of nonisothermal crystallization of polymers. I. Relationship between crystallization temperature, crystallinity, and cooling conditions, J. Appl. Polym. Sci. 16 (1972) 1077–1091.

[48] E.J. Hinch, L.G. Leal, Constitutive equations in suspension mechanics. Part 1. Approximate forms for a suspension of rigid particles affected by Brownian rotations, J. Fluid Mech. 76 (1976) 187–208.
[49] V. Verleye, F. Dupret, Prediction of fibre orientation in complex injection moulded parts, Proc. ASME Winter Annual Meeting, 28 November–3 December 1993, New Orleans, LA.
[50] J.S. Cintra, Jr.C.L. Tucker III, Orthotropic closure approximations for flow-induced fibre orientation, J. Rheol. 39 (1995) 1095–1122.
[51] R.S. Bay, Fibre Orientation in Injection Moulded Composites: A Comparison of Theory and Experiment, Ph.D. Thesis, University of Illinois at Urbana-Champaign, 1991.
[52] G.P. Tandon, G.J. Weng, The effect of aspect ratio of inclusion on elastic properties of unidirectionally aligned composites, Polymer Compos. 5 (1984) 327–333.
[53] R.A. Schapery, Thermal expansion coefficients of composite materials based on energy principles, J. Compos. Mater. 2 (1968) 380–404.
[54] J.C. Halpin, J.L. Kardos, The Halpin–Tsai equations: a review, Polym. Eng. Sci. 16 (1976) 344–352.
[55] C.W. Camacho, C.L. Tucker III, S. Yalvac, R.L. McGee, Stiffness and thermal expansion predictions for hybrid short fibre composites, Polym. Compos. 11 (1990) 229–239.
[56] R.F. Eduljee, R.L. McCullough, J.W. Gillespie, Jr, The influence of aggregated and dispersed textures on the elastic properties of discontinuous-fiber composites, Comp. Sci. Tech. 50 (1994) 381–391.
[57] R.B. Bird, R.C. Armstrong, O. Hassager, Dynamics of Polymeric Liquids: Fluid Mechanics, 2nd ed., vol.1, Wiley, New York, 1987.
[58] R.I. Tanner, Engineering Rheology, 2nd ed., Oxford Press, London, 1988.
[59] J.D. Ferry, Viscoelastic Properties of Polymers, 3rd ed., Wiley, New York, 1980.
[60] D.J. Plazek, 1995 Bingham medal address: Oh, thermorheological simplicity, wherefore art thou? J. Rheol. 40 (1996) 987–1014.
[61] N.K. Dutta, G.H. Edward, Generic relaxation spectra of solid polymers 1. Development of spectral distribution model and its application to stress relaxation of polypropylene, J. Appl. Polym. Sci. 66 (1997) 1101–1115.
[62] E.H. Lee, Stress analysis in viscoelastic bodies, Q. Appl. Math. 13 (1955) 183–190.
[63] M. Rezayat, T.E. Burton, A boundary-integral formulation for complex three-dimensional geometries, Int. J. Num. Meth. Eng. 29 (1990) 263–273.
[64] A. Couniot, L. Dheur, F. Dupret, Numerical simulation of injection moulding: nonisothermal filling of complex thin parts, including abrupt changes of thickness or bifurcations of midsurface, in: M. Cross, J.F.T. Pittman, R.D. Wood (Eds.), Proc. IMA Conf. on Mathematical Modelling for Materials Processing, Bristol, Clarendon Press, Oxford, 1991.
[65] W.F. Zoetelief, G.W.M. Peters, H.E.H. Meijer, Numerical simulation of the multi-component injection moulding process, Int. Polym. Process 12 (1997) 216–277.
[66] P.G. Bergan, M.K. Nygård, Finite elements with increased freedom in choosing shape functions, Int. J. Num. Meth. Eng. 20 (1984) 643–664.
[67] P.G. Bergan, C.A. Felippa, A triangular membrane element with rotational degrees of freedom, Comp. Meth. Appl. Mech. Eng. 50 (1985) 25–60.
[68] J.L. Batoz, P.A. Lardeur, A discrete shell triangular nine d.o.f. element for the analysis of thick to very thin plates, Int. J. Num. Meth. Eng. 28 (1989) 533–560.
[69] R. Thomas, N. McCaffrey, The prediction of real product shrinkages from a simulation of the injection molding process, SPE ANTEC 89 (1989) 371–375.